Low- and High-velocity O VI in Milky Way-like Galaxies: The Role of Stellar Feedback

Zhijie Zhang (张志杰)[1], Xiaoxia Zhang (张小霞)[1], Hui Li (李辉)[2,3], Taotao Fang (方陶陶)[1], Qingzheng Yu (余清正)[1], Yang Luo (罗阳)[4], Federico Marinacci[5,6], Laura V. Sales[7], Paul Torrey[8], and Mark Vogelsberger[9]

[1] Department of Astronomy, Xiamen University, Xiamen, Fujian 361005, People's Republic of China; zhangxx@xmu.edu.cn, fangt@xmu.edu.cn
[2] Department of Astronomy, Tsinghua University, Beijing 100084, People's Republic of China; hliastro@tsinghua.edu.cn
[3] Department of Astronomy, Columbia University, Manhattan, New York 10027, USA
[4] Department of Astronomy, Yunnan University, Kunming, Yunnan 650000, People's Republic of China
[5] Department of Physics and Astronomy "Augusto Righi", University of Bologna, Via Gobetti 93/2, I-40129 Bologna, Italy
[6] INAF, Astrophysics and Space Science Observatory Bologna, Via P. Gobetti 93/3, I-40129 Bologna, Italy
[7] Department of Physics and Astronomy, University of California, Riverside, 900 University Avenue, Riverside, CA 92521, USA
[8] Department of Astronomy, University of Virginia, 530 McCormick Road, Charlottesville, VA 22903, USA
[9] Department of Physics and Kavli Institute for Astrophysics and Space Research, Massachusetts Institute of Technology, Cambridge, MA 02139, USA

Received 2023 October 9; revised 2023 November 23; accepted 2023 November 27; published 2024 February 1

Abstract

Milky Way-type galaxies are surrounded by a warm-hot gaseous halo containing a considerable amount of baryons and metals. The kinematics and spatial distribution of highly ionized ion species such as O VI can be significantly affected by supernova (SN) explosions and early (pre-SN) stellar feedback (e.g., stellar winds, radiation pressure). Here we investigate effects of stellar feedback on O VI absorptions in Milky Way−like galaxies by analyzing the suites of high-resolution hydrodynamical simulations under the framework of SMUGGLE, a physically motivated subgrid interstellar medium and stellar feedback model for the moving-mesh code AREPO. We find that the fiducial run with the full suite of stellar feedback and moderate star formation activities can reasonably reproduce Galactic O VI absorptions observed by space telescopes such as the Far-Ultraviolet Spectroscopic Explorer, including the scale height of low-velocity ($|v_{\rm LSR}| < 100\ {\rm km\,s^{-1}}$) O VI, the column density–line width relation for high-velocity ($100\ {\rm km\,s^{-1}} \leqslant |v_{\rm LSR}| < 400\ {\rm km\,s^{-1}}$) O VI, and the cumulative O VI column densities. In contrast, model variations with more intense star formation activities deviate from observations further. Additionally, we find that the run considering only SN feedback is in broad agreement with the observations, whereas in runs without SN feedback this agreement is absent, which indicates a dominant role of SN feedback in heating and accelerating interstellar O VI. This is consistent with the current picture that interstellar O VI is predominantly produced by collisional ionization where mechanical feedback can play a central role. In contrast, photoionization is negligible for O VI production owing to the lack of high-energy ($\gtrsim 114\ {\rm eV}$) photons required.

Unified Astronomy Thesaurus concepts: High-velocity clouds (735); Interstellar medium (847); Warm ionized medium (1788); Circumgalactic medium (1879); Ultraviolet spectroscopy (2284)

1. Introduction

The multiphase gas within and surrounding galaxies including the Milky Way (MW) is an essential ingredient of galactic ecosystems that govern the galaxy evolution and may contain a significant amount of baryons and metals in the form of the cold ($T \lesssim 10^4\ {\rm K}$), warm ($T \sim 10^5$–$10^6\ {\rm K}$), and hot ($T \gtrsim 10^6\ {\rm K}$) gaseous phases (e.g., Putman et al. 2012; Tumlinson et al. 2017, and references therein). The existence of a warm–hot Galactic corona was originally proposed by Spitzer (1956) to provide pressure confinement to the neutral clouds that are ~1 kpc above the Galactic plane, and it was later confirmed by detections of the soft X-ray background (e.g., Bowyer et al. 1968) and interstellar O VI absorptions (e.g., Jenkins & Meloy 1974; York 1974). Spitzer (1956) also pointed out that such diffuse gas can be studied via the resonance doublet absorption lines of lithium-like ions, e.g., O VI, N V, and C IV. Plasmas in the temperature range of about $(1$–$5) \times 10^5\ {\rm K}$ traced by these species can be produced via moderate shocks or rapid cooling of hotter coronal gas probed in X-rays. The O VI $\lambda\lambda 1032, 1038$ doublet is of special significance owing to the large oscillator strengths (Morton 2003) and high cosmic abundance of oxygen. Under the condition of collisionally ionized equilibrium, O VI peaks in abundance at the temperature of $\sim 3 \times 10^5\ {\rm K}$ (Sutherland & Dopita 1993).

The first large-scale surveys of O VI absorption in the MW were made by the Far Ultraviolet Spectroscopic Explorer (FUSE; Moos et al. 2000; Sahnow et al. 2000). FUSE detections of O VI absorption lines toward extragalactic objects (e.g., active galactic nuclei (AGNs)/quasars) and stars in the Galactic disk, Galactic halo, and Magellanic Clouds reveal a widespread but irregular distribution of interstellar O VI with a column density of $\log(N/{\rm cm^{-2}}) \sim 13.0$–$14.8$ (e.g., Savage et al. 2000; Howk et al. 2002a; Savage et al. 2003; Sembach et al. 2003; Wakker et al. 2003; Oegerle et al. 2005; Bowen et al. 2008; Sarma et al. 2017). The O VI absorbers detected by FUSE and Hubble Space Telescope (HST) along the lines of sight (LOS) of quasars/stars move at various velocities with respect to the local standard of rest (LSR), i.e., $|v_{\rm LSR}|$ ranges from <100 to $\gtrsim 400\ {\rm km\,s^{-1}}$ (e.g., Murphy et al. 2000; Sembach et al. 2000, 2003; Fox et al. 2006; Collins et al. 2007; Shull et al. 2011).

Low-velocity (e.g., $|v_{\rm LSR}| < 100\ {\rm km\,s^{-1}}$) O VI is believed to be an extension of the Galactic disk, inflated owing to its relatively high temperature, and can be well approximated by an

---

exponentially declined layer with a midplane density of $\lesssim 2 \times 10^8\,\mathrm{cm}^{-3}$ and a scale height of ~ 2.3–4 kpc (e.g., Savage et al. 2000, 2003; Zsargó et al. 2003; Indebetouw & Shull 2004; Savage & Wakker 2009). In contrast, the nature of high-velocity (e.g., $100\,\mathrm{km\,s^{-1}} \leqslant |v_{\mathrm{LSR}}| < 400\,\mathrm{km\,s^{-1}}$) O VI and intermediate- and low-velocity ions (e.g., O I, C II, Si II, Mg II, Si III, C IV, Si IV) and atoms, the so-called high-velocity clouds (HVCs), is still debated, largely due to the highly uncertain distances for most cases. While some high-velocity O VI features are spatially and kinematically associated with known H I structures (e.g., Complex C and the Magellanic Steam), some have no neutral counterparts detected (e.g., Nicastro et al. 2003; Sembach et al. 2003; Collins et al. 2004; Fox et al. 2004; Collins et al. 2005). In addition, the covering fraction of high-velocity O VI ($\gtrsim 60\%$; e.g., Sembach et al. 2003; Fox et al. 2006) is found to be higher than that of neutral and moderately ionized HVCs ($\sim 20\%$–40% for H I, C IV, and Si IV; e.g., Lockman 2002; Herenz et al. 2013), indicating a spatially more extended distribution for highly ionized HVCs. Despite the multiple origins proposed for HVCs, for example, the Galactic fountain (e.g., Shapiro & Field 1976; Bregman 1980; Fraternali & Binney 2006), materials stripped or ejected from satellite galaxies (e.g., Putman 2004; Herenz et al. 2013), and accretion from the intergalactic medium (IGM; e.g., Kereš & Hernquist 2009; Fraternali et al. 2015), the spatial distribution and kinematics of high-velocity O VI are probably dominantly governed by the fountain model, which proposes that gas circulation in the halo is powered by stellar feedback, e.g., stellar winds and supernova (SN) explosions. Such a scenario is also supported by recently observed rainlike inflows and collimated outflows (e.g., Lehner et al. 2022; Marasco et al. 2022).

O VI absorptions for low-redshift galaxies have been extensively studied by HST and FUSE (e.g., Tripp & Savage 2000; Tripp et al. 2000; Danforth & Shull 2005; Lehner et al. 2006; Prochaska et al. 2011; Savage et al. 2011; Tumlinson et al. 2011; Fox et al. 2013; Stocke et al. 2013; Mathes et al. 2014; Peeples et al. 2014; Johnson et al. 2015; Kacprzak et al. 2015; Prochaska et al. 2019; Tchernyshyov et al. 2022). Strong O VI absorptions have been preferentially detected around star-forming galaxies, with an average O VI column density of $\log(N/\mathrm{cm}^{-2}) \sim 14.5$ (e.g., Tumlinson et al. 2011), indicating a strong impact of star formation activities on the global properties of warm gaseous halo traced by O VI . Additionally, the covering fraction of O VI was found to depend on the inclination angle of galaxies and to follow a bimodal distribution that peaks within $\sim 30°$ of the galaxy minor axis and $\sim 10°$–$20°$ of the major axis (e.g., Kacprzak et al. 2015), consistent with a circumgalactic medium (CGM) originating from major-axis-fed inflows/recycled gas and from minor-axis-driven outflows, i.e., a scenario also revealed by cooler gaseous phases traced by Mg II absorptions (e.g., Bouché et al. 2012; Kacprzak et al. 2012). Those observational evidences highlight the influence of star formation activities and stellar/AGN feedback in shaping the spatial distribution of O VI-bearing gas of external galaxies.

Stellar feedback, i.e., injection of substantial amounts of energy and angular momentum into the interstellar medium (ISM) via early (pre-SN) feedback and SN explosions, is likely to leave imprints on the properties of gaseous halos (e.g., Appleby et al. 2021; Mina et al. 2021). O VI ions probably trace matter in the interfaces between the cooler ionized/neutral clouds and hotter gas and can thus serve as indirect probes of stellar feedback

(e.g., Lehner et al. 2011). Hydrodynamical simulations are powerful tools for studying the ISM/CGM, and given that multiscale physical processes are involved in galaxy formation, subgrid models are often used to implement small-scale processes such as star formation, metal mixing and transport, and stellar feedback (e.g., Cen & Ostriker 1992; Agertz et al. 2013; Hopkins et al. 2014; Li et al. 2017; Hopkins et al. 2018; Li et al. 2018; Smith et al. 2018; Marinacci et al. 2019). Those subgruid models are parameterized and tuned to reproduce the observations, which means that feedback energy is treated as a free parameter despite its well-known importance (e.g., Barbani et al. 2023). A variety of simulations have shown that stellar feedback can have a significant impact on physical properties such as kinematics, column densities, and total content of O VI (e.g., Hummels et al. 2013; Marasco et al. 2015; Liang et al. 2016; Fielding et al. 2017; Li & Tonnesen 2020).

Stars and MUltiphase Gas in GaLaxiEs (SMUGGLE; Marinacci et al. 2019) is a physically motivated subgrid ISM and stellar feedback model for the moving-mesh code AREPO (Springel 2010) and has been widely used since its development (e.g., Kannan et al. 2020; Burger et al. 2022; Sivasankaran et al. 2022; Barbani et al. 2023). It has successfully reproduced the hydrogen emission-line profile (Smith et al. 2022), constant-density cores in dwarf galaxies (Jahn et al. 2023), and, in particular, realistic cold ISM and star cluster properties in isolated and merging galaxies (Li et al. 2020, 2022). In this paper, we test whether the SMUGGLE model can reproduce observations of warm O VI gas in and around the MW, and we investigate how the properties of O VI gas are affected by stellar feedback (e.g., early feedback and SN explosions) by analyzing the suites of simulations presented in Li et al. (2020, hereafter L20).

The paper is structured as follows. Section 2 briefly introduces the SMUGGLE model and L20's simulation and generates synthetic observations of O VI absorptions. Section 3 presents results and discussion on O VI properties for different feedback model variations, as well as comparison with the observations and some caveats. Section 4 summarizes the main conclusions.

2. Methodology

We analyze a suite of hydrodynamic simulations of isolated MW-sized galaxies presented in L20 under the SMUGGLE framework (Marinacci et al. 2019). We refer the reader to the original papers for details of the model and the simulations. Below we give a brief overview of the SMUGGLE model and L20's simulations and describe the methodology we use to create mock observations of O VI absorptions toward background sources, following Fang et al. (2002). The basic idea is to generate random LOS across the simulated region and obtain the temperature, baryon density, and velocity distributions along the LOS. Then, O VI ion density can be derived from the metallicity and ionization fraction, from which the optical depth along the LOS and thus the synthetic spectrum can be obtained. Finally, the column densities O VI and Doppler b-parameters for HVCs and low-velocity clouds (LVCs) can be calculated from the profile of the O VI absorption line.

2.1. The SMUGGLE Galaxy Formation Model

The SMUGGLE model incorporates physical processes such as gravity, hydrodynamics, gas cooling and heating, star formation, and stellar feedback and is able to resolve the

Table 1
Initial Setup of the Simulation Performed in L20

Parameter	Description	Value
M_{total}	Total mass in $M_\odot$	1.6×10^{12}
M_{disk}	Gaseous disk mass in $M_\odot$	9×10^9
m_g	The mass resolution of the gas cell in $M_\odot$	1.4×10^3
L	Simulated box size in kpc	600
r_g	Scale length of gaseous disk in kpc	6
ϵ_g	Minimum gravitational softening length of gas cells in pc	3.6
n_{th}	Density threshold for star formation in cm^{-3}	100

Table 2
Summary of the Six Model Variations in L20's Simulations

Run	ϵ_{ff}	Radiation and Winds	SN
SFE1	0.01	Yes	Yes
SFE10	0.1	Yes	Yes
SFE100	1.0	Yes	Yes
Nofeed	0.01	No	No
Rad	0.01	Yes	No
SN	0.01	No	Yes

multiphase gas structure of the ISM. Star particles are formed in cold, dense, and self-gravitating molecular gas reaching a density threshold of $n_{\text{th}} = 100 \, \text{cm}^{-3}$. The local star formation rate (SFR) for star-forming gas cells is controlled by the star formation efficiency per freefall time ϵ_{ff}, i.e., $\dot{M}_* = \epsilon_{\text{ff}} M_{\text{gas}} / \tau_{\text{ff}}$, with M_{gas} the gas mass and τ_{ff} the freefall time of the gas cell.

The model implements various channels of stellar feedback, including photoionization, radiation pressure, energy, and momentum injection from stellar winds and from SNe, which are categorized into two types:

1. *SN feedback*—injects large amounts of energy and momentum into the ISM. The event number of Type II SNe at each time step is obtained by integrating the Chabrier (2003) initial mass function, and the event rate of Type Ia SNe is calculated using a delay time distribution (Vogelsberger et al. 2013).

2. *Early (pre-SN) feedback*—includes radiative feedback and stellar winds. Photoionization and radiation pressure from young massive stars, namely radiative feedback, can impact the ionization state and offer pressure on surrounding gas and thus represent a source of momentum. The energy and momentum injection via stellar winds from young massive OB stars and older populations—asymptotic giant branch stars—are calculated from the mass loss of the two types of stars, and the former provides another channel of early feedback.

L20 performed a suite of high-resolution, isolated galactic disk simulations using the SMUGGLE model. Incorporated with explicit gas cooling and heating over a wide range of temperatures ($10–10^8$ K), the thermodynamical properties of the multiphase ISM are well studied. The simulations encompass a cubic region of 600 kpc on each side and cover the entire galaxy, with the z-axis perpendicular to the galactic disk plane. The initial conditions of the simulation are the same as those of Marinacci et al. (2019). It contains an MW-sized galaxy of $1.6 \times 10^{12} \, M_\odot$, which is composed of a stellar bulge and disk, a gaseous disk, and a dark matter halo, all with masses similar to those of the MW (see Bland-Hawthorn & Gerhard 2016, and references therein). The gaseous disk has an initial mass of $\sim 9 \times 10^9 \, M_\odot$, and the density decreases exponentially with a scale length of 6 kpc. The initial setup leads to a gas fraction of roughly 10% within a radius of $R = 8.5$ kpc. The mass resolution reaches $1.4 \times 10^3 \, M_\odot$ per gas cell, corresponding to the highest-resolution run in Marinacci et al. (2019). Gravitational softening is adaptive for gas cells, with a minimum value of ~ 3.6 pc. Table 1 lists the main parameters that characterize the initial condition of the simulations.

In L20, we performed six simulations with different subgrid models (feedback channels) and parameters (ϵ_{ff}). The model variations are summarized in Table 2 and detailed below.

1. SFE1—fiducial run in M19 with star formation efficiency of $\epsilon_{\text{ff}} = 0.01$ and all stellar feedback channels.
2. SFE10—the same as SFE1, but with $\epsilon_{\text{ff}} = 0.1$.
3. SFE100—the same as SFE1, but with $\epsilon_{\text{ff}} = 1$.
4. Nofeed—the same as SFE1, except with no stellar feedback.
5. Rad—the same as SFE1, except with only early feedback via stellar winds and radiation.
6. SN—the same as SFE1, except with only SN feedback.

2.2. Mock Observations

To generate synthetic observational data, we build a mock galactic coordinate system consistent with that of the MW. Specifically, we place the observer at the location of the Sun, i.e., 8.2 kpc away from the center of the simulated galaxy (Bland-Hawthorn & Gerhard 2016). To avoid selection effects due to a single observer in a specific location, four observers at different off-center locations are situated on the galactic disk, each 8.2 kpc away from the galactic center and 90° apart from each other (similar to the eight off-center locations in Zheng et al. 2020). We define galactic longitude l and latitude b similar to those of the galaxy.

For each given set of (l, b) and distance D of the star/quasar to the observer, we trace the LOS across the simulated region using the yt analysis toolkit (http://yt-project.org; Turk et al. 2011), which enables us to obtain gas properties such as temperatures, velocities in the LSR reference frame, and baryon densities along the LOS. To directly compare the properties of the warm gas in the simulated galaxy with observations, we convert hydrogen density to O VI density, and then to O VI column density. For a grid of gas temperatures ($T \sim 10^3–10^7$ K) and hydrogen densities ($n_{\text{H}} \sim 10^{-8}–10^6 \, \text{cm}^{-3}$), we adopt the CLOUDY code (version C17.02; Ferland et al. 1998, 2017) to calculate the ionization fraction $f_{\text{O VI}}(T, n_{\text{H}})$ of O VI, taking into account the ultraviolet (UV) background radiation from quasars and galaxies (Haardt & Madau 1996). The number density of O VI can be derived via

$$n(\text{O VI}) = n_{\text{H}} A_{\text{O}} \left(\frac{Z}{Z_\odot} \right) f_{\text{O VI}}(T, n_{\text{H}}), \qquad (1)$$

where Z is the gas metallicity that is set to be the solar, i.e., $Z = Z_\odot$, and $A_{\text{O}} = 4.9 \times 10^{-4}$ is the abundance of oxygen (Asplund et al. 2009).

Take a random sightline at $(l, b) = (0°, 30°)$ as an example. Figure 1 shows the gas temperature, LSR velocity, baryon
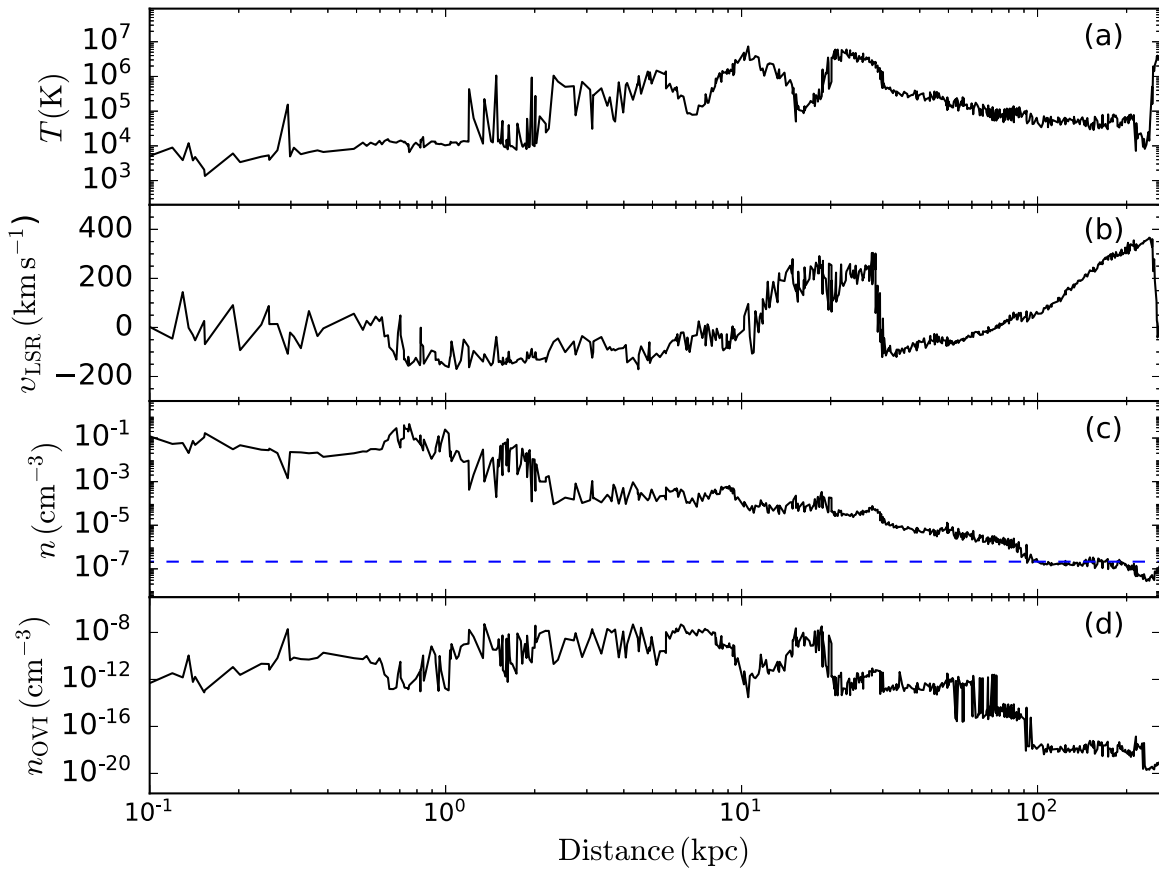
Figure 1. (a) Gas temperature, (b) velocity in the LSR reference frame, (c) baryon number density, and (d) O VI number density along the sightline $(l, b) = (0°, 30°)$ in galactic coordinates to an observation at the Sun's location. The blue dashed line in panel (c) denotes the mean baryon density of the universe (see the text for details).

number density, and O VI number density along the sightline for the fiducial SFE1 run. The temperature of the gas along the LOS spans a wide range of $\sim 10^3$–10^7 K, and the LSR velocity ranges from roughly -200 to $400\,\mathrm{km\,s^{-1}}$. The baryon density exhibits a downward trend as the distance increases, reaching the cosmic mean value of $\sim 2.1 \times 10^{-7}\,\mathrm{cm^{-3}}$ at $D \sim 100\,\mathrm{kpc}$ (blue dashed line). O VI density generally traces the variation of gas temperature for distances $\lesssim 50\,\mathrm{kpc}$. The reason is that for temperature of $\lesssim 5 \times 10^5$ K the ionization fraction of O VI is a monotonic function of the gas temperature.

The number density of O VI ions along the LOS provides a direct measure to the optical depth (τ) around the O VI $\lambda 1032$ line, from which the mock spectrum of a background source (e.g., a star or quasar) can be obtained (e.g., Spitzer 1978; Zhang et al. 1997; Fang et al. 2002). We consider the effects of line broadening and line-center shift caused by both the Hubble velocity and the peculiar velocity of the gas along the LOS (e.g., Fang et al. 2002). The original spectrum is convolved with the FUSE line-spread function to account for the instrumental broadening (b_{inst}), i.e., $b = \sqrt{b_{\mathrm{therm}}^2 + b_{\mathrm{inst}}^2}$, with b_{therm} the thermal broadening and $b_{\mathrm{inst}} \sim 12$–$15\,\mathrm{km\,s^{-1}}$ (Moos et al. 2000; Sembach et al. 2003). Gaussian noise is further considered with the mean of 0 and the standard deviation of 0.01. The final synthetic spectrum, or the transmission $\exp(-\tau)$, is shown as the black solid line in Figure 2, for a background source placed at a distance of 260 kpc and in the direction of $(l, b) = (0°, 30°)$, the same LOS as in Figure 1. Multiple absorption components can be seen with $|v_{\mathrm{LSR}}| \sim 30$–$300\,\mathrm{km\,s^{-1}}$, consistent with a wide spread of velocity for gas along the LOS shown in Figure 1(b).

We adopt the apparent optical depth (AOD) method to calculate the column density (N), centroid velocity, and Doppler b-parameter for low- and high-velocity O VI by assuming that the absorption profile is not saturated (e.g., Savage & Sembach 1991; Sembach et al. 2003). For low-velocity O VI, the column density, centroid velocity, and line width are calculated with fixed integration limits of $(v_-, v_+) = (-100, 100)\,\mathrm{km\,s^{-1}}$ (the magenta band in Figure 2). For high-velocity O VI, the integration limits rely on O VI velocity structures (e.g., Sembach et al. 2003) and are extracted from the cyan bands in Figure 2, which include regions with $\exp(-\tau) < 0.95$ and $100\,\mathrm{km\,s^{-1}} \leqslant |v_{\mathrm{LSR}}| < 400\,\mathrm{km\,s^{-1}}$. Here 0.95 is chosen somewhat arbitrarily to exclude false "absorption features" caused by noise. The two cyan bands indicate two high-velocity components with integration limits of the velocity set by the boundaries of each cyan band. We define $|v_{\mathrm{LSR}}| < 100\,\mathrm{km\,s^{-1}}$ as LVCs and $100\,\mathrm{km\,s^{-1}} \leqslant |v_{\mathrm{LSR}}| < 400\,\mathrm{km\,s^{-1}}$ as HVCs.

Figure 3 displays an all-sky map of O VI column density derived from the fiducial SFE1 run, for low-velocity (top), high-velocity (middle), and total gas (bottom) observed at the Sun's location. As can be seen, low-velocity O VI is widespread in the sky, with column densities of $\log(N/\mathrm{cm^{-2}}) \gtrsim 14$, and stretches to a high galactic latitude of $|b| \gtrsim 60°$. In comparison, high-velocity O VI is generally located near the galactic disk, with $\log(N/\mathrm{cm^{-2}}) \gtrsim 15$, and gradually declines toward higher galactic latitudes. Such a "disklike" structure for high-velocity O VI does not appear in the other five runs, which suggests that the spatial distribution of O VI strongly depends on the subgrid models of stellar feedback. However, it is challenging to detect O VI absorption at low latitudes (e.g., $|b| \lesssim 25°$) owing to
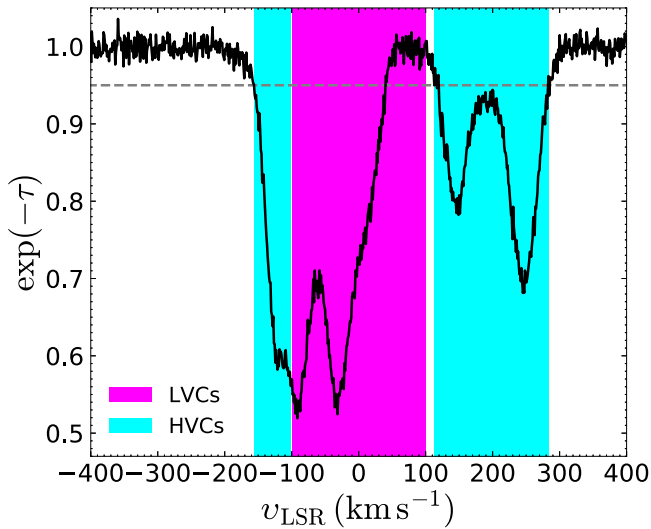
Figure 2. An example of synthetic O VI absorption spectrum (the black solid line) and identification of low- and high-velocity O VI components. Velocities between -100 and 100 km s^{-1} are identified as low-velocity components by the magenta band marks. High-velocity components are shown as the cyan bands, with velocities exceeding 100 km s^{-1} and $\exp(-\tau) < 0.95$. The gray dashed line marks $\exp(-\tau) = 0.95$.
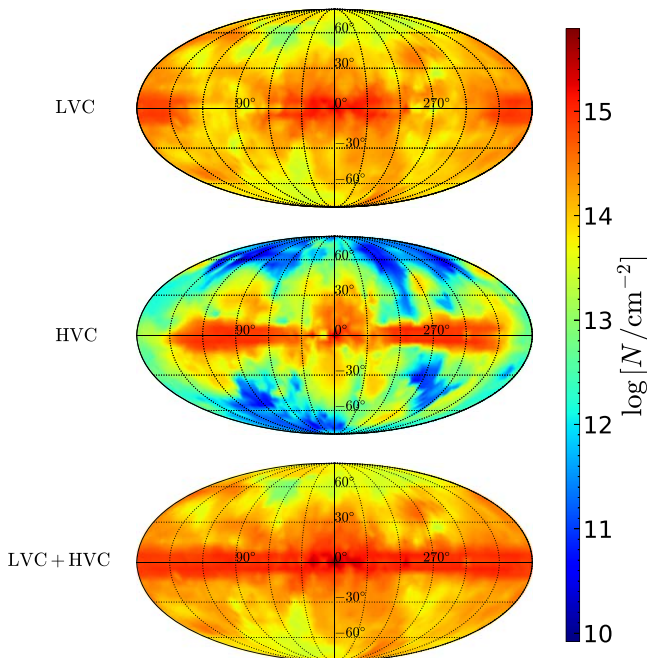

Figure 3. All-sky Mollweide projection of O VI column densities for LVCs ($|v_{LSR}| < 100$ km s^{-1}; top panel), HVCs (100 km s$^{-1} \leqslant |v_{LSR}| < 400$ km s^{-1}; middle panel), and total clouds ($|v_{LSR}| < 400$ km s^{-1}; bottom panel), for an observer located at the Sun's position.

severe ultraviolet extinction for extragalactic objects (e.g., Sembach et al. 2003; Wakker et al. 2003). Therefore, currently it is unavailable to distinguish those models via the observed spatial distribution of O VI.

3. Results and Discussion

We derive O VI properties of the simulated galaxy viewed by four internal off-center observers for the fiducial SFE1 run in Sections 3.1–3.3. The fiducial results are then compared with the other five model variations in Section 3.4, where

the impact of subgrid model/parameter variations is illustrated. Section 3.5 presents results from an external view to compare with observations of external galaxies, which is followed by some caveats in Section 3.6.

3.1. The Scale Height of LVCs

The mock observation of the simulated galaxy in Section 2 provides measurement to the O VI column density along an arbitrary LOS across the simulated region. A certain number of sightlines allow us to explore the spatial distribution of the O VI-bearing gas, which can be compared with the observations. Savage & Wakker (2009) collected column densities of O VI and other species along 139 LOSs toward stars and quasars and found that low-velocity O VI in the MW is well fitted by an exponentially declined disk model with a scale height of $h \sim 2.6 \pm 0.6$ kpc. To compare our results with those observations, we generate random LOS according to the following settings.

For each of the four off-center observers, we randomly generate 4×139 LOSs across the simulated galaxy toward quasars or stars, and thus the total sightline number is $4 \times 4 \times 139 = 2224$. Here 139 is the LOS number collected by Savage & Wakker (2009), among which 109 (30) are toward stars (quasars). We assign the same ratio of numbers for sightlines toward quasars to that toward stars, i.e., 480 (1744) out of the 2224 LOSs are toward quasars (stars). The quasars are situated at a distance of 260 kpc (e.g., the virial radius of the galaxy), and the galactic latitude is randomly drawn at $|b| > 20°$ since detectable sightlines toward quasars are usually observationally unavailable at $|b| \lesssim 20°$. The stars are placed in random directions with a distance randomly drawn from 1 to 10 kpc in logarithmic space. This distance range is consistent with the observational data collected by Savage & Wakker (2009). O VI column densities for LVCs are derived according to the AOD method presented in Section 2.2. We further set a detection limit of O VI column density $\log(N/\text{cm}^{-2}) \geqslant 13.23$ for sightlines toward both quasars and stars (e.g., Savage & Wakker 2009), and there are 1601 O VI absorbers detected along the 2224 LOSs, as the gray circles in Figure 4 show. Our results generally agree with the observations of low-velocity O VI (blue circles; Savage & Wakker 2009).

To quantify the distribution of low-velocity O VI, we adopt a simple disk model (e.g., Savage et al. 1990, 2000; Yao & Wang 2005; Savage & Wakker 2009), i.e., the number density declines exponentially away from the midplane (or the galactic disk), and the density at a height z below/above the midplane can be expressed as

$$n(z) = n_0 e^{-|z|/h}, \qquad (2)$$

where n_0 is the mean density in the midplane and h is the scale height of the O VI disk. Then, the column density (N) along the LOS can be simply derived from the integration of Equation (2), and its projection along the z-axis is

$$N \sin|b| = n_0 h (1 - e^{-|z|/h}). \qquad (3)$$

The formula reveals a monotonic relation between $N \sin|b|$ and $|z|$, for $|z| \lesssim h$; for $|z| \gg h$, $N \sin|b|$ eventually approaches a stable value of $n_0 h$.

To perform a reasonable minimum$-\chi^2$ fitting to our mock data (gray circles in Figure 4), we divide the x-axis into bins. Red circles with error bars show the mean values and standard
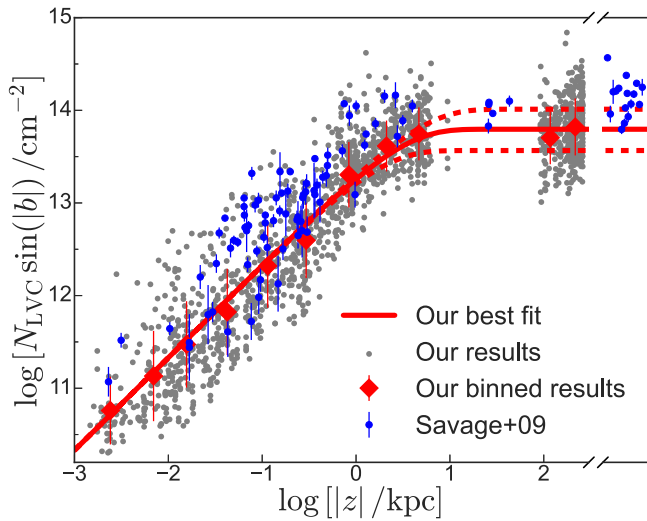
Figure 4. Projected O VI column density along the z-axis vs. height to the galactic plane for LVCs in the SFE1 run. The gray circles represent our mock results, and the red diamonds are our binned results with 1σ error bars. The red solid line is the best-fit model to the red diamonds, and the dashed lines enclose the 1σ confidence region accounting for the errors of the scale height. The blue circles are results revealed by observations (Savage & Wakker 2009).

deviations in each bin. These binned data are then fitted to the disk model, with the best-fitting profile shown as the red solid line. Our best-fitting model has a scale height of $h = 2.9^{+1.9}_{-1.2}$ kpc, well consistent with the MW observations of 2.6 ± 0.5 kpc (Savage & Wakker 2009) considering the 1σ errors. The best-fit parameters and a comparison with observations are listed in Table 3.

3.2. Column Density–Line Width Relation

A correlation between the column density and the line width of O VI absorbers was first reported by Heckman et al. (2002) and has been found in various environments, including the Galactic disk and halo (Jenkins 1978a, 1978b; Savage et al. 2003; Bowen et al. 2008; Lehner et al. 2011; Sarma et al. 2017), HVCs (Sembach et al. 2003), and Magellanic Clouds (Howk et al. 2002a, 2002b; Hoopes et al. 2002; Pathak et al. 2011). Collisional processes should be responsible for the linear proportionality between the column density and b-parameter since the column density linearly scales with the gas flow velocity in the collisional ionization scenario (see discussions in Heckman et al. 2002; Sembach et al. 2003). Below we investigate the column density–line width relation for low- and high-velocity O VI, which are then compared with the observations.

Figure 5 depicts the column density versus Doppler parameter distribution for low-velocity O VI. Each data point is obtained from a randomly drawn sightline at $|b| > 20°$, from four off-center observers toward quasars/stars, as described in Section 3.1. O VI column densities span $\log(N/\mathrm{cm}^{-2}) \sim 13.2$–15.2 with a median value of 13.8, and the line width follows a Gaussian-like distribution within $b \sim 13$–106 km s^{-1} and peaks at $\sim$47 km s^{-1}. The median values are listed in the fourth and fifth columns in Table 3. The distribution and median value of the column density are well consistent with the observations (the gray histogram and dotted line; Savage & Wakker 2009). For most of the sightlines, the line width is broader than that caused by thermal motion of O VI ions, which corresponds to $b_{\mathrm{therm}} \sim 17.7$ km s^{-1} for a gas temperature of 3×10^5 K, implying significant nonthermal

motions, e.g., inflows, outflows, and turbulence. This could be responsible for the distorted or no relation between the column density and line width. Although no correlation between N and b is also expected for photoionized gas, given the high energy ($\sim$114 eV) required for ionizing photons, it is implausible for most of the O VI ions to be produced by photoionization, except for extreme conditions with a hard radiation field and a very low gas density (see, e.g., Sembach et al. 2003).

For HVCs, O VI λ1032 absorptions have been detected by FUSE at $\geqslant 3\sigma$ confidence levels along 59 out of the 102 sightlines, among which 100 are toward extragalactic objects and two toward halo stars (Sembach et al. 2003). To make a direct comparison with their results, we randomly generate a total of $16 \times 59 = 944$ sightlines from four off-center observers, where 59 is the number of sightlines with detected O VI absorption reported by Sembach et al. (2003). The background quasars are placed at a distance of 260 kpc, and the galactic latitude is limited to $|b| > 20°$. Accounting for the detected high-velocity O VI properties (see Table 1 in Sembach et al. 2003), our mock detections need to satisfy the following conditions: (i) the integration interval $v_+ - v_- \geqslant 50$ km s^{-1}, (ii) O VI column density $\log(N_{\mathrm{HVC}}/\mathrm{cm}^{-2}) \geqslant 13.06$, and (iii) O VI line width $b_{\mathrm{HVC}} \geqslant 16$ km s^{-1}. This results in 339 detections (blue filled circles in Figure 6) of high-velocity O VI out of the 944 sightlines, with a detection rate (339/944) lower than that (84/102) given by observations.

Our column densities and line widths of high-velocity O VI occupy a similar parameter space to the observations (Sembach et al. 2003), with $b \sim 16$–107 km s^{-1} and $\log(N/\mathrm{cm}^{-2}) \sim 13.1$–14.8. The median values are also consistent with the real data considering the 1σ uncertainties, i.e., $b \sim 33.0 \pm 18.8$ km s^{-1} versus 40.0 ± 13.1 km s^{-1} and $\log(N/\mathrm{cm}^{-2}) \sim 13.8 \pm 0.4$ versus 14.0 ± 0.3 (see the seventh and eighth columns in Table 3). Unlike the symmetric distribution for LVCs, the line widths for high-velocity O VI peak at $b \lesssim 20$ km s^{-1}, suggesting that nonthermal motions for high-velocity O VI might be less significant than for its low-velocity counterparts. In addition, unlike the random distribution for LVCs, there is a significant positive correlation between the column density and Doppler b-value for high-velocity O VI, still in line with the FUSE observations of the MW (Sembach et al. 2003). Such a correlation may support collisional ionization instead of photoionization as the dominant mechanism for the production of high-velocity O VI (see, e.g., Heckman et al. 2002). Moreover, photoionization models underproduce observed O VI column densities by an order of magnitude (e.g., Sembach et al. 2003), also lending support to the collisional ionization origin.

3.3. Cumulative Column Density

We note that Zheng et al. (2020) investigated cumulative O VI column densities from an inside-out view of MW analogs selected from the Figuring Out Gas & Galaxies In Enzo (FOGGIE) simulation (Peeples et al. 2019). To make a direct comparison with their results, we adopt the same method as that of Zheng et al. (2020) and randomly generate a total of 1000 LOSs with $|b| > 20°$ for the four off-center observers. For each of the sightlines, we calculate the column density as a function of the distance r to the observer by integrating Equation (1) over r.

The median profile and the 16th and 84th percentiles are displayed as the blue solid line and band in Figure 7. Despite a

Table 3
Properties of Low- and High-velocity O VI Clouds for the Six Runs in L20's Simulation and Comparison with the Observations

Model/Obs.	h (kpc)	n_0 (cm^{-3})	$\log(n_0 h)$ (cm^{-2})	b_{LVC} (km s^{-1})	$\log N_{LVC}$ (cm^{-2})	b_{HVC} (km s^{-1})	$\log N_{HVC}$ (cm^{-2})
SFE1	$2.9^{+1.9}_{-1.2}$	6.92×10^{-9}	13.79 ± 0.16	47.38 ± 15.18	13.81 ± 0.38	33.02 ± 18.81	13.80 ± 0.37
SFE10	$1.3^{+1.3}_{-0.7}$	1.39×10^{-8}	13.77 ± 0.18	47.62 ± 17.29	13.97 ± 0.43	20.17 ± 9.56	13.86 ± 0.30
SFE100	$1.9^{+1.6}_{-0.9}$	7.64×10^{-9}	$13.67^{+0.16}_{-0.17}$	38.09 ± 14.10	13.79 ± 0.41	24.21 ± 12.41	13.66 ± 0.29
Nofeed	$2.0^{+1.0}_{-0.7}$	4.10×10^{-9}	$13.41^{+0.10}_{-0.11}$	39.56 ± 18.81	13.58 ± 0.30	⋯	⋯
Rad	$0.5^{+1.6}_{-0.5}$	1.41×10^{-8}	$13.36^{+0.14}_{-0.15}$	39.59 ± 16.27	13.60 ± 0.41	27.28 ± 5.31	13.64 ± 0.21
SN	$2.7^{+2.2}_{-1.3}$	1.19×10^{-8}	$13.99^{+0.20}_{-0.19}$	47.89 ± 17.90	14.04 ± 0.42	31.95 ± 20.11	13.92 ± 0.36
Savage+09	2.6 ± 0.5	1.64×10^{-8}	$14.12^{+0.07}_{-0.08}$	⋯	14.15 ± 0.35	⋯	⋯
Sembach+03	⋯	⋯	⋯	⋯	⋯	40.00 ± 13.14	13.97 ± 0.33

Note. Column (1): the six model variations of the simulation presented in L20 (the second to seventh rows), or the observations of LVCs and HVCs by Savage & Wakker (2009) and Sembach et al. (2003), respectively (the last two rows). Columns (2)–(4): the best-fit parameters of the disk model for low-velocity O VI. Columns (5)–(6): the median column density and line width for low-velocity O VI. Columns (7)–(8): the median column density and line width for high-velocity O VI.
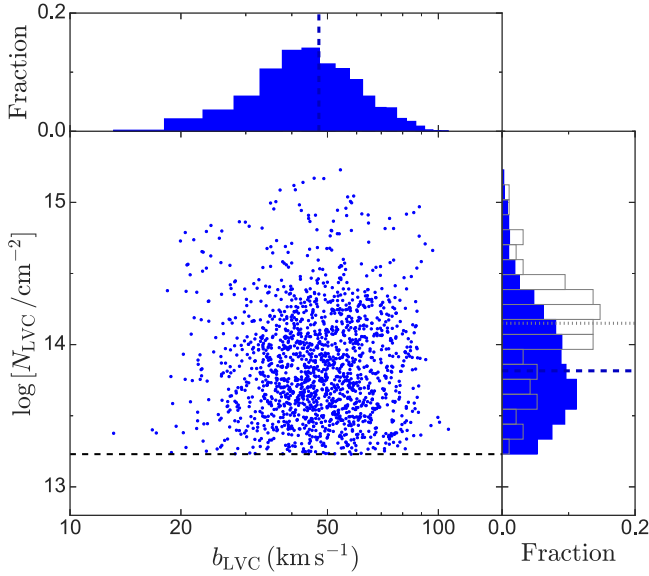

Figure 5. Column density and line width distribution of O VI-bearing LVCs in the fiducial SFE1 run. The blue histograms give the probability distribution of the column density (right) and line width (top), with the median values denoted by the blue dashed lines, as compared with the observations shown as the gray histogram and gray dotted line (Savage & Wakker 2009).

Figure 6. Similar to Figure 5, but for high-velocity O VI. The gray triangles denotes FUSE observations of HVCs (Sembach et al. 2003).

systematic offset between our results (blue solid line) and observations of LVCs toward quasars/stars (green plus signs and magenta circles; Savage et al. 2003; Savage & Wakker 2009), about half of the observational data points are consistent with our 1σ uncertainties (blue band). The extrapolation of our results to larger distances, i.e., $\log(N/\mathrm{cm}^{-2}) \sim 14$, also agrees with HVC observations toward quasars/stars (Sembach et al. 2003) at $r > 100$ kpc. Given that those observations only include low- or high-velocity O VI, each set of the observations may represent a lower limit when compared to our results. The large discrepancy at smaller distances ($r \lesssim 0.3$ kpc) could arise from small-scale clumps and cavities in the ISM induced by SN explosions and other feedback processes (Li et al. 2020), despite the small number statistics.

In contrast, Zheng et al. (2020) underproduced O VI in the halos by 1–2 orders of magnitude in the column density (gray dashed line in Figure 7),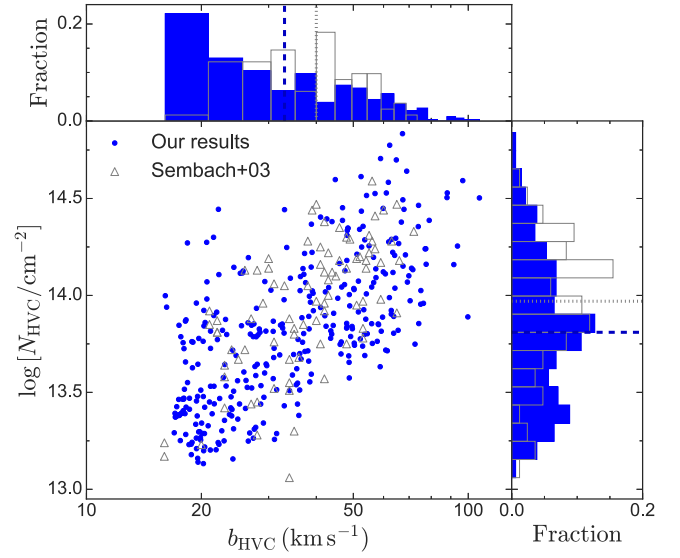 compared to our results and to the observations. The reason, as they have pointed out, could be that their simulated dark matter halos are smaller than the real case (Bland-Hawthorn & Gerhard 2016), and/or that they only consider the thermal feedback from SNe, which is unable to expel enough metals into the ISM/CGM. The consideration of the full suite of feedback processes (e.g., stellar winds, radiative feedback, and SN explosions) by the SMUGGLE model and by the fiducial run of L20's simulation could be responsible for our agreement with the real data.

3.4. Other Simulation Models

Results presented in Sections 3.1–3.3 are derived from the fiducial SFE1 run of L20's simulation. To explore how O VI absorption features are affected by different subgrid models, we consider the other five variations listed in Table 2 for comparison.

Similar to Figure 4 for the SFE1 run, Figure 8 shows $\log(N_{LVC} \sin|b|)$ versus $\log|z|$ for the other five models. While the scale height for low-velocity O VI derived from the fiducial SFE1 run is comparable to the observations (Savage & Wakker 2009), the runs with higher star formation efficiency,
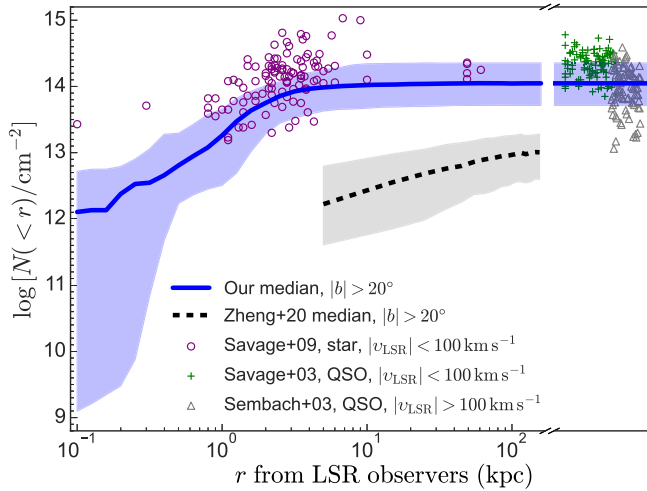
Figure 7. Profile of the cumulative O VI column density for the SFE1 run, as represented by the blue solid line and the blue band. Purple open circles, green plus signs, and gray triangles are observations of low-velocity O VI toward stars (Savage & Wakker 2009) and toward quasars (Savage et al. 2003) and high-velocity O VI toward quasars (Sembach et al. 2003), respectively. The gray dashed line and gray band are the simulation results given by Zheng et al. (2020).

e.g., SFE10 and SFE100 runs, result in smaller scale height for O VI-bearing gas. The scale height does not always decrease with increasing star formation efficiency, which is attributed to the degeneracy between the scale height (h) and midplane density (n_0). Meanwhile, the projected column density $\log(n_0 h)$ at $|z| \gg h$ decreases slightly as the star formation activity weakens. The reason is that early feedback (e.g., stellar winds, radiation pressure) that is enhanced by intense star formation blows gas and metals away. Higher star formation efficiency also leads to more SN events at a given time step, and SN feedback could also play a role. The Rad run considering only radiative feedback and stellar winds results in much lower scale height and projected column density, compared to the SFE1 run with the full suite of stellar feedback, revealing that SN feedback plays an important role in reproducing the observed spatial distribution of low-velocity O VI, i.e., SN energy and momentum injections collisionally ionize more O VI and push the warm gas farther out of the galactic disk. Indeed, the fitting result for the SN run is in nice agreement with the observations. In contrast, the run without feedback, "Nofeed," gives an overall lower density and a low scale height for low-velocity O VI.

Table 3 (the second to fourth columns) lists the best-fit parameters for the six runs and the values derived from observations (Savage & Wakker 2009), which, for a clearer view, are compared in Figure 9.

Figure 10 displays the column densities and line width distribution of low-velocity O VI for the other five model variations, which are obtained similarly to that for the SFE1 run shown in Figure 5. Similar to the SFE1 run, none of the five runs exhibit obvious correlations. The distribution and median value of O VI column density for the SN run agree very well with the observations. In contrast, the runs' lack of SN feedback (e.g., Nofeed and Rad runs) underproduce O VI, with median column densities ~0.6 dex lower. The critical impact of SN feedback is once again highlighted.

For high-velocity O VI, the column density–line width relations are displayed in Figure 11 for the other four runs,

as compared to that of the SFE1 run shown in Figure 6. The median values of the column densities and line widths for different runs are listed in the seventh and eighth columns of Table 3. The Nofeed run is not displayed because no high-velocity O VI components are detected, indicating the necessity of feedback processes to accelerate O VI particles. While the column densities of high-velocity O VI derived from different runs generally agree with the observations (Sembach et al. 2003) accounting for the uncertainties, the median values and distributions of the Doppler parameter support the SFE1 and SN runs, both including SN feedback.

The $\log(n_0 h)$ values for different model variations listed in Table 3 represent the simulated galaxy at the "present" time when the simulation is terminated. In fact, for each snapshot of the simulation, we can similarly obtain its $\log(n_0 h)$ value. In Figure 12, we present the evolution of $\log(n_0 h)$ across the simulation time for the six runs. As can be seen by comparing the SFE1, SFE10, and SFE100 runs, a larger star formation efficiency results in a downward tendency of $\log(n_0 h)$ over time. This could be attributed partly to the fast conversion of cold gas to stars, and thus less oxygen is left for O VI production via heating. Meanwhile, the stellar winds from young massive stars have an important impact on the ISM gas (Lamers & Cassinelli 1999; Muijres et al. 2012), e.g., dispersing the gas and impeding the generation of O VI ions via SN feedback heating. Consequently, the "present" value of $\log(n_0 h)$ and its 2σ confidence region for the SFE1 run marginally agree with the observations (Savage et al. 2003; Bowen et al. 2008; Savage & Wakker 2009), yet the SFE100 run deviates further. For the SFE1 and SN runs, the simulation data are available only for runtime within 0.8 and 0.5 Gyr, respectively. Based on the currently available data, the "present" $\log(n_0 h)$ values for these two runs are in better agreement with the observations than the other four model variations.

To summarize, comparison of different runs in L20's simulation with the observations of low- and high-velocity O VI favors the SFE1 and SN runs, suggesting that SN feedback is required to reproduce the O VI observations, and meanwhile early feedback associated with star formation activities should be moderate (not too strong), e.g., with star formation efficiency of $\epsilon_{\rm ff} \sim 0.01$.

3.5. Comparison with External Galaxies

Results in Sections 3.1–3.4 are viewed from off-center observers inside the simulated galaxy. Here we present results for the SFE1 run viewed from an external observer and compare with observations of external galaxies.

The left panel of Figure 13 shows the face-on view of the O VI column density map (on xy−plane). For each grid of coordinates (x, y), the column density is obtained by integrating the O VI number density in Equation (1) along the z-axis with a path length of 600 kpc, i.e., the size of the simulation box. The white dashed line denotes the virial radius of 260 kpc. The column density peaks at the center with $\log(N/\rm cm^{-2}) \sim 15.3$ and gradually declines toward the outer region, approaching a background value of $\log(N/\rm cm^{-2}) \sim 4.4$. Besides that, there is tentative evidence for structures spanning tens of kiloparsecs.

To make a direct comparison with observations of external galaxies, we plot the column density versus the impact parameter in the right panel of Figure 13. To achieve that, we generate random sightlines for both face-on and edge-on
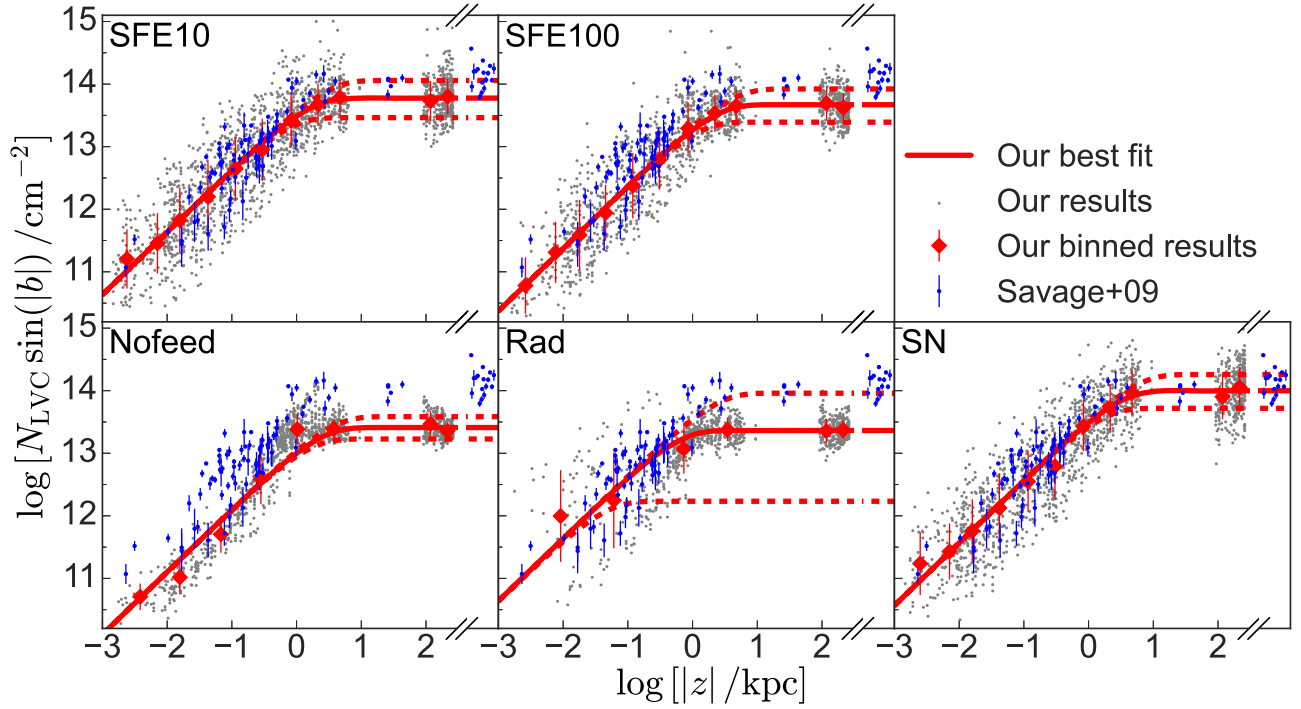
Figure 8. Distribution of the projected column densities along the z-axis vs. heights above the galactic disk for low-velocity O VI, for the other five runs as labeled in each panel. Legends are similar to those in Figure 4.
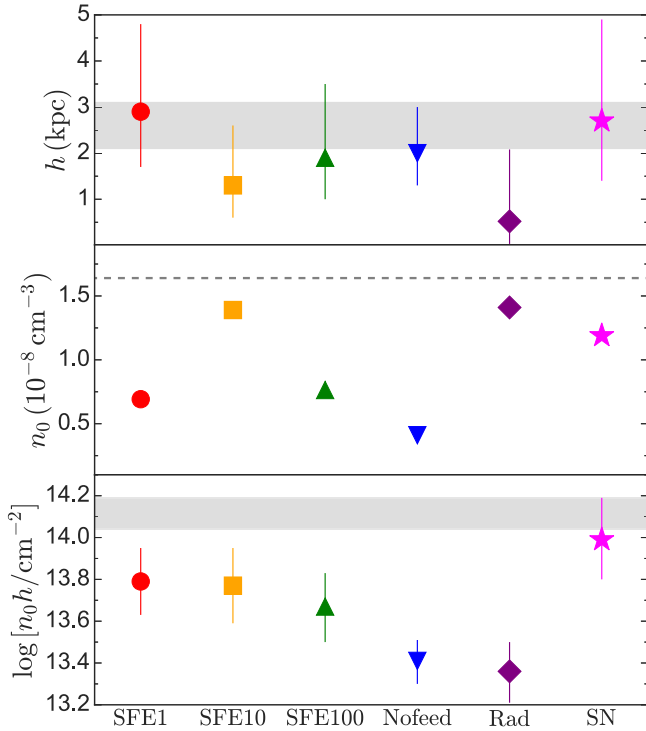

Figure 9. Comparison of the best-fit parameters (y-axes of the panels) of the disk model for the six model variations (x-axes). The gray band and dashed line are the observational constraints provided by Savage & Wakker (2009). See also the red lines in Figure 4 (the SFE1 run) and Figure 8 (the other five runs) for the fitting results and Table 3 for the best-fit parameters.

views of the simulated galaxy. The blue solid line shows the median column density, and the blue band shows the range of 5th–95th percentiles. Our results are consistent with the observations of sub- and super-L_* galaxies (Prochaska et al.

2011) for impact parameter $\lesssim 50$ kpc. Beyond that, the column density sharply declines and drops below the observational values. This happens as expected because the simulation performed by L20, as well as the SMUGGLE galaxy formation model, is for an isolated galaxy without gas supply from the IGM, which is also the shortcoming of this study. Indeed, the Galactic halo density ($\sim 10^{-4}\,\mathrm{cm}^{-3}$) suggested by observations of the Magellanic Stream (Weiner & Williams 1996) is more than one order of magnitude higher than our results ($\lesssim 10^{-5}\,\mathrm{cm}^{-3}$; Figure 1(c)) at a radius of ~ 50 kpc.

3.6. Caveats

3.6.1. Isolated Galaxy Simulation

Our results are based on L20's simulations for an isolated galaxy without gas fueling from the IGM and interactions with companion galaxies. This could lead to an underestimation of O VI column density at outer regions, e.g., $r \gtrsim 100$ kpc (see Figure 13). In addition, our high-velocity O VI clouds can only be produced via the galactic fountain, i.e., triggered by stellar feedback (e.g., Shapiro & Field 1976; Bregman 1980; Fraternali & Binney 2006). If other mechanisms such as accretion from the IGM (e.g., Kereš & Hernquist 2009; Fraternali et al. 2015) and materials stripped or ejected from satellites (e.g., Putman 2004; Herenz et al. 2013) are also responsible for the formation of high-velocity O VI, our simulation (Table 3) may underproduce high-velocity O VI content and distort its spatial distribution.

3.6.2. The Metallicity

Our results in this work are obtained under the assumption of solar metallicity for the gas when converting the number density of hydrogen to that of O VI in Equation (1). Constant metallicity is often assumed for simplicity despite the fact that
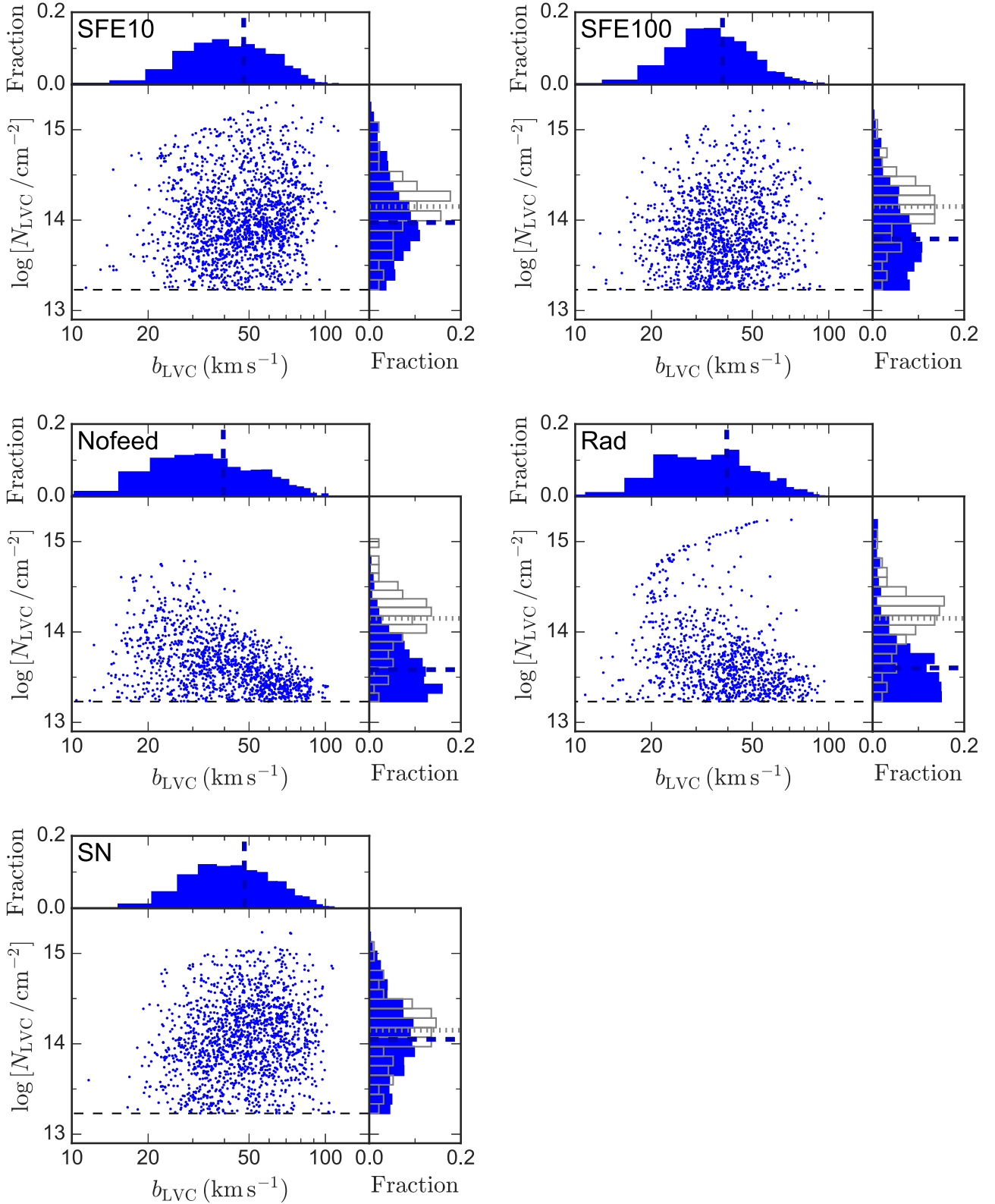
Figure 10. The column density and line width distribution for low-velocity O VI, for the other five runs as labeled in the upper left corner of each panel. Legends are similar to Figure 5.

the metallicity could differ by orders of magnitudes for different regions of the galaxy (e.g., Gutcke et al. 2017; De Cia et al. 2021). Alternatively, we quantify the effect of metallicity on the scale height evolution of low-velocity O VI for the SFE10 run in Figure 14, by setting three constant metallicities

of 1, 3, and 5 $Z_\odot$. As expected, a higher metallicity results in a larger scale height of O VI, which differs by a factor of $\lesssim 2$ for 1 and 5 $Z_\odot$ cases, comparable to the variations of the scale height across the simulation time of ~ 1 Gyr. While the SFE10 run is ruled out under the assumption of solar metallicity when
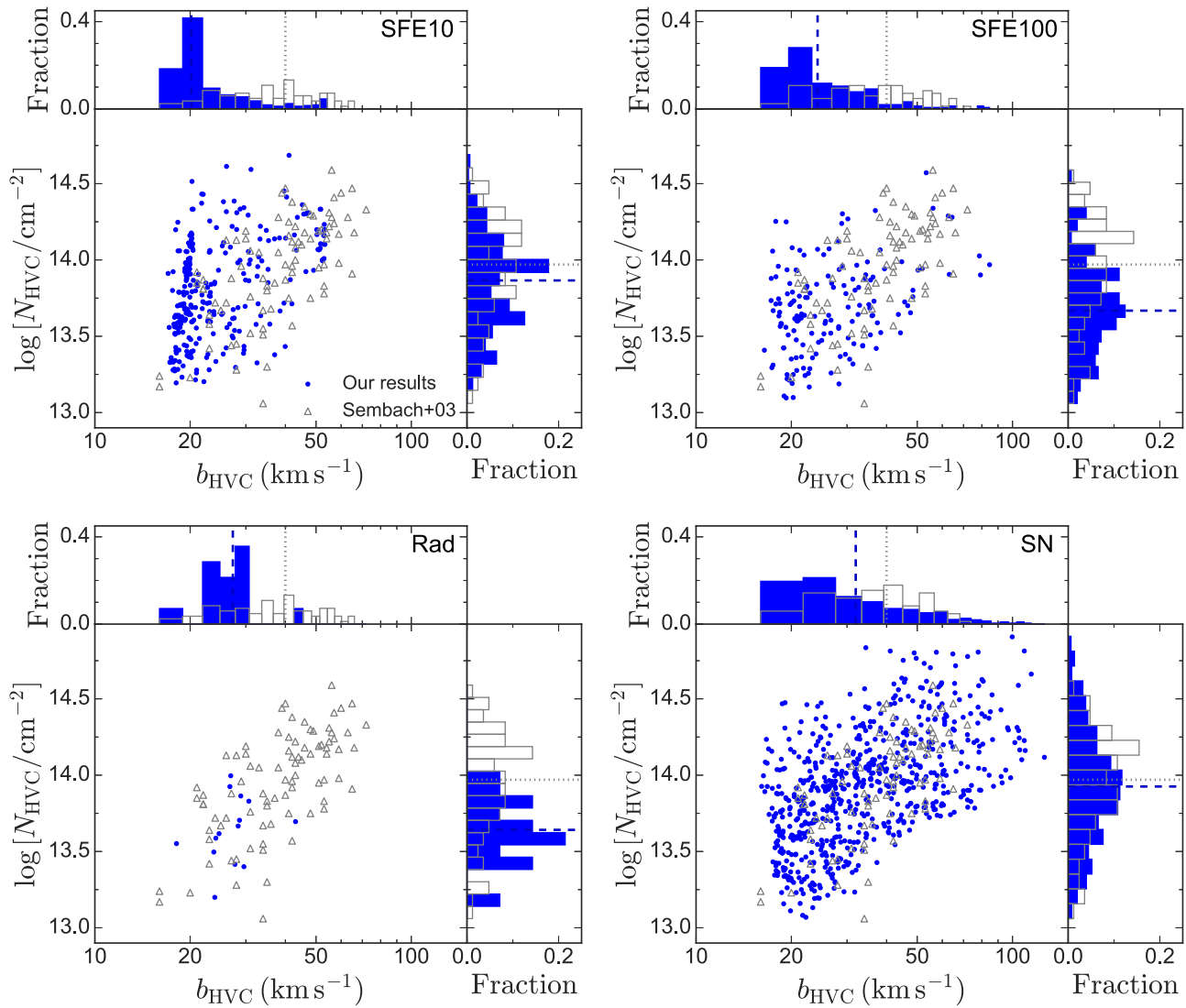
Figure 11. Column densities vs. line width distribution for high-velocity O VI for the other four model variations. Legends are similar to Figure 6. The Nofeed run is not displayed because no high-velocity O VI absorptions are detected.

compared to the observations (Savage et al. 2003; Bowen et al. 2008; Savage & Wakker 2009), higher metallicity of $5 Z_\odot$ makes the SFE10 run's results ($h = 2.3^{+2.2}_{-1.2}$ kpc) well consistent with the observations considering the errors. This indicates that, to some extent, a higher metallicity can compensate for lower O VI content caused by strong early feedback (e.g., stellar winds, radiation pressure) launched by short-lived massive stars.

3.6.3. The UV Background and Other Ionizing Sources

Our results on O VI properties of the simulated galaxies are based on Equation (1), where the ionization fraction of O VI is derived via CLOUDY (Ferland et al. 2017) modeling by taking into account extragalactic UV background radiation (Haardt & Madau 1996). While such a UV background is typically applied to IGM regions (e.g., Fang & Bryan 2001), there are alternative versions of the UV background in the literature and other potential contributions of ionizing sources, e.g., stellar radiation within the galaxy and cosmic-ray heating (Werk et al. 2014).

The spectral shape of the UV background has been shown to affect oxygen abundance (Aguirre et al. 2008) and statistics of O VI absorbers in the IGM (Oppenheimer & Davé 2009). A comparison of various UV backgrounds has been presented in Figure 1 of Mallik et al. (2023), including the one (Haardt & Madau 1996) we adopted. The energy of ~ 114 eV required for photoionizing O V corresponds to the high-energy tail of the spectral energy distribution (SED) of the background radiation field. Consequently, most O VI could be produced from collisional ionization at temperatures of $\sim 3 \times 10^5$ K rather than from photoionization at lower temperatures (e.g., Cox 2005). Moreover, the flux difference at the ionizing energy is at most ~ 0.5 dex for various frequently used UV backgrounds and should not make much difference.

Photoionization is considered as a channel of radiative stellar feedback in the framework of the SMUGGLE model, and the O VI distribution that is controlled by the ionization fraction $f_{\mathrm{O\,VI}}(T, n_{\mathrm{H}})$ in Equation (1) is affected by feedback processes in terms of heating (increasing the temperature T) and/or blowing gas away (decreasing hydrogen density n_{H}). However, the stellar radiation inside the galaxy is not directly considered in the CLOUDY modeling. The contribution of a starburst galaxy
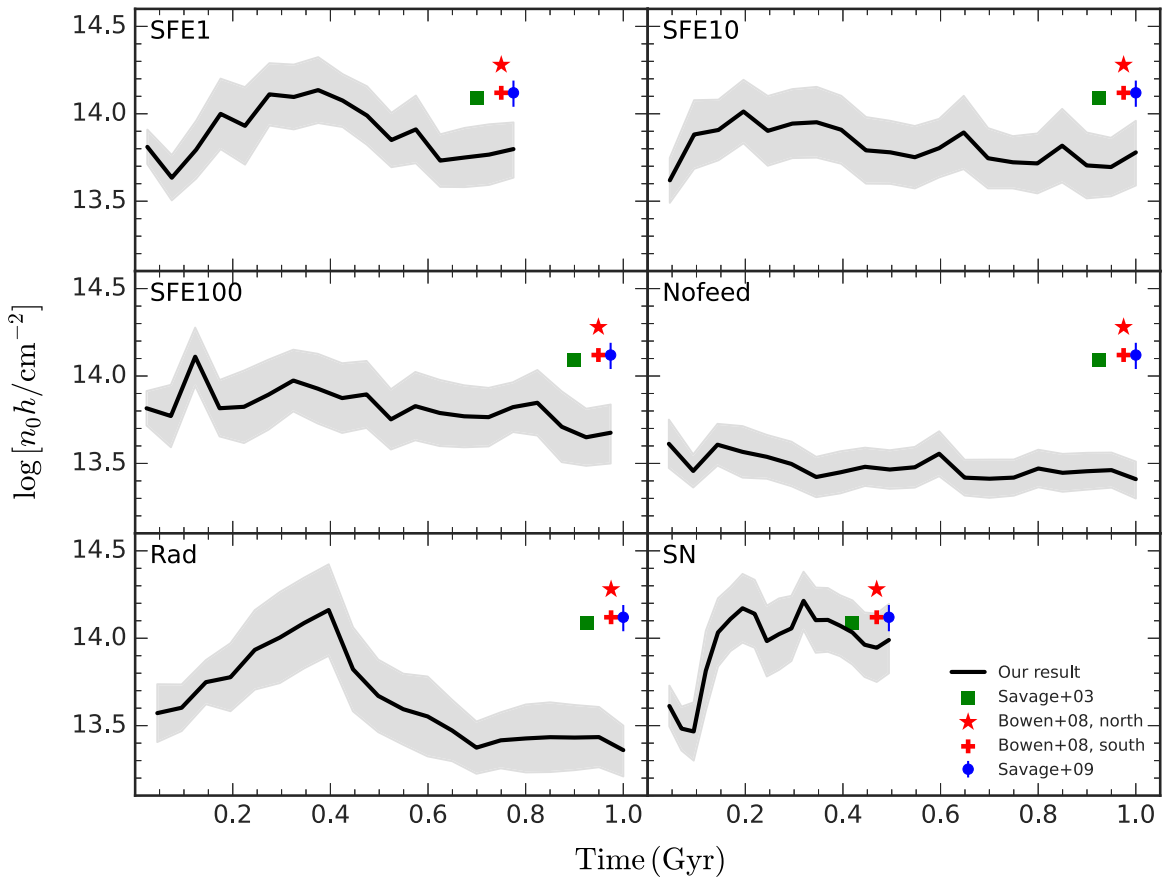
Figure 12. The evolution of $\log(n_0h)$ as a function of time for the six model variations. The black solid line is our results, with the 1σ uncertainty represented by the gray region. The symbols denote the observational $\log(n_0h)$ values of the galaxy reported by Savage et al. (2003), Bowen et al. (2008), and Savage & Wakker (2009), as labeled, which are arbitrarily shifted along the x-axis to make the comparison more clearly.

to the total ionizing photons is evaluated in Figure 13 of Werk et al. (2014). The SED of the radiation field with the contribution of the starburst galaxy with an SFR of $1\,M_\odot\,\mathrm{yr}^{-1}$ at a distance of $d = 72\,\mathrm{kpc}$ has a similarly flat slope toward higher energies ($E \gtrsim 70\,\mathrm{eV}$) and deviates ~ 0.1 dex from the Haardt & Madau (2001) UV background. While the assumed SFR is typically true for our simulated MW-like galaxy (Li et al. 2020), the distance of O VI clouds to the star-forming region spans a wide range across the halo (0–260 kpc). Figure 8 of Fox et al. (2005) compares the UV background radiation with the radiation from the MW at different locations within the Galaxy and reveals that the radiation field from the Galaxy is similar to the Haardt & Madau (1996) UV background at $E \sim 114\,\mathrm{eV}$ for a distance of $d \sim 20$–$30\,\mathrm{kpc}$. The sharp decrease of the radiation flux at 54 eV arising from the He II edge in hot stars indicates that high-energy photons of $E > 114\,\mathrm{eV}$ are very limited. Detailed CLOUDY modeling suggests that photoionization is negligible for the production of O VI despite its dependence on the radiation field adopted.

Cosmic-ray heating could serve as a crucial supplementary source of ionization and heating within the Galactic virial radius (Wiener et al. 2013). For gas densities $\gtrsim 10^{-2}\,\mathrm{cm}^{-3}$, the cosmic-ray background (CRB) can dominate over photoelectric heating for gas, accounting for a weaker dependence on the gas density for the CRB heating. Therefore, CRB could signifi-cantly enhance the density of O VI in low-density regions, although the precise number is challenging to determine

because of the poorly constrained local CRB (see discussions in Werk et al. 2014).

4. Conclusions

We study O VI properties in MW-like galaxies by analyzing the suites of simulations performed by L20 in the framework of the SMUGGLE galaxy formation model. We find that the SMUGGLE model is capable of producing consistent global properties of Galactic warm gas traced by O VI. In addition, mechanical stellar feedback is shown to have a crucial impact on the spatial distribution and kinematics of O VI absorbers. Particularly, SN feedback is necessarily required, and early feedback associated with star formation activities needs to be moderate to reproduce O VI observations. Our main findings are detailed as follows.

1. Low-velocity O VI distribution is well described by an exponentially declining disk with a scale height of $2.9^{+1.9}_{-1.2}$ kpc and $\log(n_0h/\mathrm{cm}^{-2}) = 13.79 \pm 0.16$ for the fiducial SFE1 run (with full suites of feedback processes), generally consistent with the observations. The SN run (with SN feedback only) results in a scale height well consistent with observations as well. Other runs turning off SN feedback or with higher star formation efficiencies lead to smaller values for the scale height.

2. For the SFE1 run, the column density of low-velocity O VI is distributed in the range of $\log(N/\mathrm{cm}^{-2}) \sim 13.2$–$15.2$ with a median value of ~ 13.8, consistent with observations
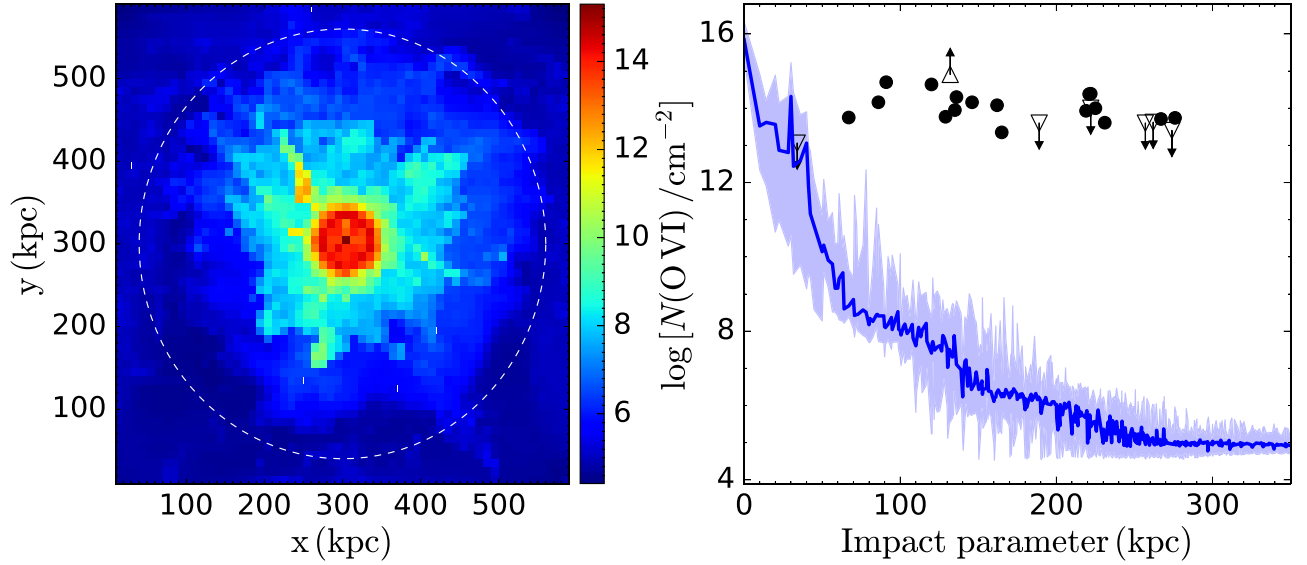
Figure 13. Left: face-on projection of O VI column density (along the z-axis) for the SFE1 run, as the color bar denotes. The white dashed line marks the galaxy's virial radius of 260 kpc. Right: O VI column density as a function of the impact parameter derived from random face-on and edge-on sightlines. The blue solid line is our median result, and the blue area denotes the 5th−95th percentile range. The black filled circles and open triangles are the observational results for sub- and super-L_* galaxies, respectively, given by Prochaska et al. (2011).
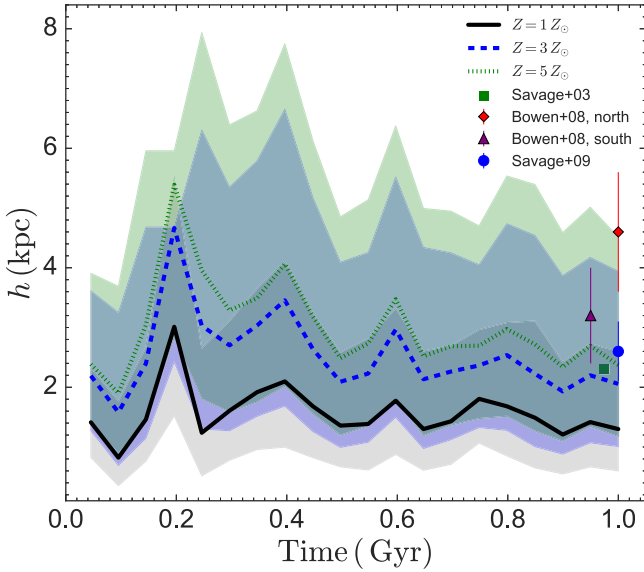
Figure 14. The evolution of the exponential scale height h of low-velocity O VI as a function of time for the SFE10 run with metallicities of 1 $Z_\odot$ (black solid line), 3 $Z_\odot$ (blue dashed line), and 5 $Z_\odot$ (green dotted line). The lines represent the median values for random sightlines described in Section 3.1, and the regions with corresponding colors represent 1σ uncertainties. The symbols with error bars are observational results reported by Savage et al. (2003), Bowen et al. (2008), and Savage & Wakker (2009), as labeled. In particular, Bowen et al. (2008) provide the scale heights of low-velocity O VI for the northern ($b > 20°$) and southern ($b < -20°$) hemispheres of the MW.

within 1σ uncertainties. The line width of low-velocity O VI follows a Gaussian-like distribution over $b \sim 13$–$106\,\mathrm{km\,s^{-1}}$ with a median value of $47.4\,\mathrm{km\,s^{-1}}$. No correlations are found between the column density and line width of low-velocity O VI for all of the model variations.

3. For high-velocity O VI in the SFE1 run, the column density spans $\log(N/\mathrm{cm^{-2}}) \sim 13.1$–$14.8$ with a median of ~ 13.8, and line width covers $b \sim 16$–$107\,\mathrm{km\,s^{-1}}$ with a median of $\sim 33\,\mathrm{km\,s^{-1}}$. A positive correlation is found between the column density and line width of high-

velocity O VI, supporting collisional ionization as the dominant mechanism for the production of high-velocity O VI. No high-velocity O VI clouds are found in the run turning off all channels of stellar feedback.

4. The profile of cumulative O VI column density generally agrees with observations for the SFE1 run. The evolution of $\log(n_0 h)$ as a function of simulation time also supports the SFE1 and SN runs when comparing to observations.

5. We cannot reproduce observations of the column density profile for external galaxies owing to the lack of accretion in our simulations, suggesting that accretion is an important part of galaxy evolution modeling.

Overall, the observed Galactic O VI properties can be reasonably reproduced with simulations of isolated MW-like disks based on the SMUGGLE model with novel treatment of ISM and stellar feedback, in complement to L20's findings of its success in producing realistic cold ISM. A test of its ability in reproducing hotter Galactic gas traced by highly ionized metal species such as O VII and O VIII is deferred to a future work. One shortcoming of the SMUGGLE model could be the lack of cosmological gas accretion. The next generation of the SMUGGLE model intends to involve cosmological simulations with zoom-in of individual objects and will serve as a powerful tool for predicting galactic structure, outflows, and CGM properties.

Software: yt (Turk et al. 2011), CLOUDY (Ferland et al. 2017), Astropy (Astropy Collaboration et al. 2018), Matplotlib (Hunter 2007), SciPy (Virtanen et al. 2020).

ORCID iDs

Xiaoxia Zhang (张小霞) ● https://orcid.org/0000-0003-4832-9422

Hui Li (李辉) ● https://orcid.org/0000-0002-1253-2763

Taotao Fang (方陶陶) ● https://orcid.org/0000-0002-2853-3808

Qingzheng Yu (余清正) ● https://orcid.org/0000-0003-3230-3981

Yang Luo (罗阳) ● https://orcid.org/0000-0002-2243-2790

Federico Marinacci ● https://orcid.org/0000-0003-3816-7028

Laura V. Sales ● https://orcid.org/0000-0002-3790-720X

Paul Torrey ● https://orcid.org/0000-0002-5653-0786

Mark Vogelsberger ● https://orcid.org/0000-0001-8593-7692

References

Agertz, O., Kravtsov, A. V., Leitner, S. N., & Gnedin, N. Y. 2013, ApJ, 770, 25
Aguirre, A., Dow-Hygelund, C., Schaye, J., & Theuns, T. 2008, ApJ, 689, 851
Appleby, S., Davé, R., Sorini, D., Storey-Fisher, K., & Smith, B. 2021, MNRAS, 507, 2383
Asplund, M., Grevesse, N., Sauval, A. J., & Scott, P. 2009, ARA&A, 47, 481
Astropy Collaboration, Price-Whelan, A. M., Sipőcz, B. M., et al. 2018, AJ, 156, 123
Barbani, F., Pascale, R., Marinacci, F., et al. 2023, MNRAS, 524, 4091
Bland-Hawthorn, J., & Gerhard, O. 2016, ARA&A, 54, 529
Bouché, N., Hohensee, W., Vargas, R., et al. 2012, MNRAS, 426, 801
Bowen, D. V., Jenkins, E. B., Tripp, T. M., et al. 2008, ApJS, 176, 59
Bowyer, C. S., Field, G. B., & Mack, J. E. 1968, Natur, 217, 32
Bregman, J. N. 1980, ApJ, 236, 577
Burger, J. D., Zavala, J., Sales, L. V., et al. 2022, MNRAS, 513, 3458
Cen, R., & Ostriker, J. P. 1992, ApJL, 399, L113
Chabrier, G. 2003, PASP, 115, 763
Collins, J. A., Shull, J. M., & Giroux, M. L. 2004, ApJ, 605, 216
Collins, J. A., Shull, J. M., & Giroux, M. L. 2005, ApJ, 623, 196
Collins, J. A., Shull, J. M., & Giroux, M. L. 2007, ApJ, 657, 271
Cox, D. P. 2005, ARA&A, 43, 337
Danforth, C. W., & Shull, J. M. 2005, ApJ, 624, 555
De Cia, A., Jenkins, E. B., Fox, A. J., et al. 2021, Natur, 597, 206
Fang, T., & Bryan, G. L. 2001, ApJL, 561, L31
Fang, T., Bryan, G. L., & Canizares, C. R. 2002, ApJ, 564, 604
Ferland, G. J., Chatzikos, M., Guzmán, F., et al. 2017, RMxAA, 53, 385
Ferland, G. J., Korista, K. T., Verner, D. A., et al. 1998, PASP, 110, 761
Fielding, D., Quataert, E., McCourt, M., & Thompson, T. A. 2017, MNRAS, 466, 3810
Fox, A. J., Lehner, N., Tumlinson, J., et al. 2013, ApJ, 778, 187
Fox, A. J., Savage, B. D., & Wakker, B. P. 2006, ApJS, 165, 229
Fox, A. J., Savage, B. D., Wakker, B. P., et al. 2004, ApJ, 602, 738
Fox, A. J., Wakker, B. P., Savage, B. D., et al. 2005, ApJ, 630, 332
Fraternali, F., & Binney, J. J. 2006, MNRAS, 366, 449
Fraternali, F., Marasco, A., Armillotta, L., & Marinacci, F. 2015, MNRAS, 447, L70
Gutcke, T. A., Stinson, G. S., Macciò, A. V., Wang, L., & Dutton, A. A. 2017, MNRAS, 464, 2796
Haardt, F., & Madau, P. 1996, ApJ, 461, 20
Haardt, F., & Madau, P. 2001, XXIst Moriond Astrophysics Meeting, Clusters of Galaxies and the High Redshift Universe Observed in X-Rays, ed. D. M. Neumann & J. T. T. Van, 64
Heckman, T. M., Norman, C. A., Strickland, D. K., & Sembach, K. R. 2002, ApJ, 577, 691
Herenz, P., Richter, P., Charlton, J. C., & Masiero, J. R. 2013, A&A, 550, A87
Hoopes, C. G., Sembach, K. R., Howk, J. C., Savage, B. D., & Fullerton, A. W. 2002, ApJ, 569, 233
Hopkins, P. F., Kereš, D., Oñorbe, J., et al. 2014, MNRAS, 445, 581
Hopkins, P. F., Wetzel, A., Kereš, D., et al. 2018, MNRAS, 480, 800

Howk, J. C., Savage, B. D., Sembach, K. R., & Hoopes, C. G. 2002a, ApJ, 572, 264
Howk, J. C., Sembach, K. R., Savage, B. D., et al. 2002b, ApJ, 569, 214
Hummels, C. B., Bryan, G. L., Smith, B. D., & Turk, M. J. 2013, MNRAS, 430, 1548
Hunter, J. D. 2007, CSE, 9, 90
Indebetouw, R., & Shull, J. M. 2004, ApJ, 607, 309
Jahn, E. D., Sales, L. V., Marinacci, F., et al. 2023, MNRAS, 520, 461
Jenkins, E. B. 1978a, ApJ, 219, 845
Jenkins, E. B. 1978b, ApJ, 220, 107
Jenkins, E. B., & Meloy, D. A. 1974, ApJL, 193, L121
Johnson, S. D., Chen, H.-W., & Mulchaey, J. S. 2015, MNRAS, 449, 3263
Kacprzak, G. G., Churchill, C. W., & Nielsen, N. M. 2012, ApJL, 760, L7
Kacprzak, G. G., Muzahid, S., Churchill, C. W., Nielsen, N. M., & Charlton, J. C. 2015, ApJ, 815, 22
Kannan, R., Marinacci, F., Vogelsberger, M., et al. 2020, MNRAS, 499, 5732
Kereš, D., & Hernquist, L. 2009, ApJL, 700, L1
Lamers, H. J. G. L. M., & Cassinelli, J. P. 1999, Introduction to Stellar Winds (Cambridge: Cambridge Univ. Press)
Lehner, N., Howk, J. C., Marasco, A., & Fraternali, F. 2022, MNRAS, 513, 3228
Lehner, N., Savage, B. D., Wakker, B. P., Sembach, K. R., & Tripp, T. M. 2006, ApJS, 164, 1
Lehner, N., Zech, W. F., Howk, J. C., & Savage, B. D. 2011, ApJ, 727, 46
Li, H., Gnedin, O. Y., & Gnedin, N. Y. 2018, ApJ, 861, 107
Li, H., Gnedin, O. Y., Gnedin, N. Y., et al. 2017, ApJ, 834, 69
Li, H., Vogelsberger, M., Bryan, G. L., et al. 2022, MNRAS, 514, 265
Li, H., Vogelsberger, M., Marinacci, F., Sales, L. V., & Torrey, P. 2020, MNRAS, 499, 5862
Li, M., & Tonnesen, S. 2020, ApJ, 898, 148
Liang, C. J., Kravtsov, A. V., & Agertz, O. 2016, MNRAS, 458, 1164
Lockman, F. J. 2002, ApJL, 580, L47
Mallik, S., Srianand, R., Maitra, S., Gaikwad, P., & Khandai, N. 2023, MNRAS, 523, 2296
Marasco, A., Debattista, V. P., Fraternali, F., et al. 2015, MNRAS, 451, 4223
Marasco, A., Fraternali, F., Lehner, N., & Howk, J. C. 2022, MNRAS, 515, 4176
Marinacci, F., Sales, L. V., Vogelsberger, M., Torrey, P., & Springel, V. 2019, MNRAS, 489, 4233
Mathes, N. L., Churchill, C. W., Kacprzak, G. G., et al. 2014, ApJ, 792, 128
Mina, M., Shen, S., Keller, B. W., et al. 2021, A&A, 655, A22
Moos, H. W., Cash, W. C., Cowie, L. L., et al. 2000, ApJL, 538, L1
Morton, D. C. 2003, ApJS, 149, 205
Muijres, L. E., Vink, J. S., de Koter, A., Müller, P. E., & Langer, N. 2012, A&A, 537, A37
Murphy, E. M., Sembach, K. R., Gibson, B. K., et al. 2000, ApJL, 538, L35
Nicastro, F., Zezas, A., Elvis, M., et al. 2003, Natur, 421, 719
Oegerle, W. R., Jenkins, E. B., Shelton, R. L., Bowen, D. V., & Chayer, P. 2005, ApJ, 622, 377
Oppenheimer, B. D., & Davé, R. 2009, MNRAS, 395, 1875
Pathak, A., Pradhan, A. C., Sujatha, N. V., & Murthy, J. 2011, MNRAS, 412, 1105
Peeples, M. S., Corlies, L., Tumlinson, J., et al. 2019, ApJ, 873, 129
Peeples, M. S., Werk, J. K., Tumlinson, J., et al. 2014, ApJ, 786, 54
Prochaska, J. X., Burchett, J. N., Tripp, T. M., et al. 2019, ApJS, 243, 24
Prochaska, J. X., Weiner, B., Chen, H. W., Mulchaey, J., & Cooksey, K. 2011, ApJ, 740, 91
Putman, M. E. 2004, in High Velocity Clouds, ed. H. van Woerden et al. (Dordrecht: Kluwer), 101
Putman, M. E., Peek, J. E. G., & Joung, M. R. 2012, ARA&A, 50, 491
Sahnow, D. J., Moos, H. W., Ake, T. B., et al. 2000, ApJL, 538, L7
Sarma, R., Pathak, A., Murthy, J., & Sarma, J. K. 2017, MNRAS, 464, 4927
Savage, B. D., Edgar, R. J., & Diplas, A. 1990, ApJ, 361, 107
Savage, B. D., Lehner, N., & Narayanan, A. 2011, ApJ, 743, 180
Savage, B. D., & Sembach, K. R. 1991, ApJ, 379, 245
Savage, B. D., Sembach, K. R., Jenkins, E. B., et al. 2000, ApJL, 538, L27
Savage, B. D., Sembach, K. R., Wakker, B. P., et al. 2003, ApJS, 146, 125
Savage, B. D., & Wakker, B. P. 2009, ApJ, 702, 1472
Sembach, K. R., Savage, B. D., Shull, J. M., et al. 2000, ApJL, 538, L31
Sembach, K. R., Wakker, B. P., Savage, B. D., et al. 2003, ApJS, 146, 165
Shapiro, P. R., & Field, G. B. 1976, ApJ, 205, 762
Shull, J. M., Stevens, M., Danforth, C., et al. 2011, ApJ, 739, 105
Sivasankaran, A., Blecha, L., Torrey, P., et al. 2022, MNRAS, 517, 4752
Smith, A., Kannan, R., Tacchella, S., et al. 2022, MNRAS, 517, 1
Smith, M. C., Sijacki, D., & Shen, S. 2018, MNRAS, 478, 302

Spitzer, L. 1978, Physical Processes in the Interstellar Medium (New York: Wiley)
Spitzer, L. J. 1956, ApJ, 124, 20
Springel, V. 2010, MNRAS, 401, 791
Stocke, J. T., Keeney, B. A., Danforth, C. W., et al. 2013, ApJ, 763, 148
Sutherland, R. S., & Dopita, M. A. 1993, ApJS, 88, 253
Tchernyshyov, K., Werk, J. K., Wilde, M. C., et al. 2022, ApJ, 927, 147
Tripp, T. M., & Savage, B. D. 2000, ApJ, 542, 42
Tripp, T. M., Savage, B. D., & Jenkins, E. B. 2000, ApJL, 534, L1
Tumlinson, J., Peeples, M. S., & Werk, J. K. 2017, ARA&A, 55, 389
Tumlinson, J., Thom, C., Werk, J. K., et al. 2011, Sci, 334, 948
Turk, M. J., Smith, B. D., Oishi, J. S., et al. 2011, ApJS, 192, 9

Virtanen, P., Gommers, R., Oliphant, T. E., et al. 2020, NatMe, 17, 261
Vogelsberger, M., Genel, S., Sijacki, D., et al. 2013, MNRAS, 436, 3031
Wakker, B. P., Savage, B. D., Sembach, K. R., et al. 2003, ApJS, 146, 1
Weiner, B. J., & Williams, T. B. 1996, AJ, 111, 1156
Werk, J. K., Prochaska, J. X., Tumlinson, J., et al. 2014, ApJ, 792, 8
Wiener, J., Zweibel, E. G., & Oh, S. P. 2013, ApJ, 767, 87
Yao, Y., & Wang, Q. D. 2005, ApJ, 624, 751
York, D. G. 1974, ApJL, 193, L127
Zhang, Y., Anninos, P., Norman, M. L., & Meiksin, A. 1997, ApJ, 485, 496
Zheng, Y., Peeples, M. S., O'Shea, B. W., et al. 2020, ApJ, 896, 143
Zsargó, J., Sembach, K. R., Howk, J. C., & Savage, B. D. 2003, ApJ, 586, 1019